

High-speed Atomic Force Microscopy

メタデータ	言語: eng 出版者: 公開日: 2017-10-03 キーワード (Ja): キーワード (En): 作成者: メールアドレス: 所属:
URL	http://hdl.handle.net/2297/35149

High-speed Atomic Force Microscopy

Running title: High-speed AFM

Toshio Ando

Department of Physics, Kanazawa University, Kakuma-machi, Kanazawa 920-1192, Japan

TEL: +81 (0)76-264-5663

FAX: +81 (0)76-264-5739

E-MAIL: tando@staff.kanazawa-u.ac.jp

Corresponding Author: Toshio Ando

Keywords

Atomic force microscopy, high-speed AFM, realtime imaging, dynamics of proteins, biomolecular processes, bioimaging

Abstract

High-speed atomic force microscopy (HS-AFM) has been developed as a nano-dynamics visualization technique. This microscopy permits the direct observation of structure dynamics and dynamic processes of biological molecules in physiological solutions, at subsecond to sub-100 ms temporal resolution and ~ 2 nm lateral and 0.1 nm vertical resolution. Importantly, tip-sample interactions do not disturb the biomolecules' functions. Various functioning proteins including myosin V walking on an actin filament and bacteriorhodopsin responding to light have been successfully visualized with HS-AFM. In the quest for understanding the functional mechanisms of proteins, inferences no longer have to be made from static snapshots of molecular structures and dynamic behavior of optical markers attached to proteins. High-resolution molecular movies obtained from HS-AFM observations reveal the details of molecules' dynamic behavior in action, without the need for intricate analyses and interpretations. In this review, I first describe the fundamentals behind the achieved high imaging rate and low invasiveness to samples, and then highlight recent imaging studies. Finally, future studies are briefly described.

Introduction

Directly observing individual protein molecules in action at high spatiotemporal resolution has long been a holy grail for biological science. An ideal microscopy technique performing this type of observation has to meet all of the following conditions (see Table 1): (i) in-liquid specimen imaging, (ii) high spatial resolution, (iii) high temporal resolution, (iv) low invasiveness to the specimen, and (v) direct imaging of the specimen without the use of markers (in other words, the morphology of the specimen itself is resolved). For example, fluorescence microscopy that is reinforced by superresolution techniques surpassing the diffraction limit [1] meets the first through the fourth conditions, but is never able to satisfy the fifth condition in principle. Although many efforts have been carried out to develop liquid electron microscopy techniques capable of observing non-stained biological specimens in solutions [2], the electron dose required to achieve high contrast and spatial resolution instantaneously kills the sample. Solving this problem is a highly difficult, if not impossible, task. Atomic force microscopy (AFM) meets the first, second, and fifth conditions and moderately meets the fourth condition, but its temporal resolution (30 s at its highest level) is too low to trace the dynamics of biological molecules in real time. However, when I started to develop high-speed AFM (HS-AFM) two decades ago, the low temporal resolution of AFM had intuitively seemed to me to be an issue that could be circumvented, although I had no rational strategies at that time.

AFM was originally invented to visualize atoms on solid surfaces [3] but is now routinely used in biological sciences [4, 5] for high-resolution imaging of biological samples under physiological conditions [6, 7], as well as force measurements to estimate the strength of intra- and intermolecular bonds at the single-molecule level [8, 9] and the elasticity of biological surfaces [10-12]. Soon after the advent of AFM, several groups attempted to observe dynamic biological events despite the very low imaging rate of AFM: Paul Hansma and colleagues observed the clotting process by fibrin at 1 min intervals [13], and a group including one of the inventors of AFM (Gerd Binnig) also tried to image the dynamic processes of live cells being infected by a virus [14] and the binding of antibodies to the S-layer of bacterial cells [15]. In 1992, Binnig predicted that “in biology, use of the force microscope will probably become quite common because of its ability to deliver films of processes” [16]. However, we had to wait 16 years until this prediction came true.

In 2008, the instrumentation development for HS-AFM was completed [17]. Toward this completion, various techniques and devices were developed: small cantilevers [18-20], optical beam deflection (OBD) detectors for detecting deflection of a small cantilever [20, 21], fast amplitude detectors [17, 20], fast scanners [17, 22, 23], a counterbalance method to avoid the generation of unwanted vibrations of the scanner [20, 23], an active damping method for the z-scanner [24], a compensator for drift in the cantilever excitation efficiency [25], and a new feedback controller [25]. Since the completion of HS-AFM instrumentation development, the

technique's ability to reveal the structure dynamics and dynamic processes of proteins has been demonstrated continuously [26-30]. As such, there is no doubt that this new microscopy will be widely used in biological research in the near future. This review does not intend to describe specific HS-AFM techniques, but instead provides the fundamentals behind the high imaging rate and low invasiveness to the sample, highlights recent imaging studies of proteins, and outlines ongoing and future studies to expand the scope of HS-AFM's application to biological studies. For technical details of the instrumentation, more application studies, and experimental procedures for imaging, see reviews [17], [31], and [32], respectively.

Fundamentals behind high imaging rate

Principles of tapping mode AFM

Among a number of operation modes, HS-AFM employs the tapping mode [33]. In this mode, the cantilever is oscillated at its first resonant frequency f_c . A stylus probe attached to the free end of the cantilever is intermittently brought into contact with the sample, which significantly reduces the friction between the tip and sample during lateral scanning of the sample stage. The mechanical response of the cantilever upon contact, i.e., change in the cantilever's oscillation amplitude, is measured, and then the sample stage is moved in the z-direction to recover the amplitude back to its initial set point value through feedback control (see Fig. 1). This series of operations is repeated many times for different sample surface points during lateral scanning of the sample stage. Consequently, the movement of the sample stage traces the sample surface, and therefore, the feedback controller output at each xy position represents the sample height at the position. Thus, the sample surface topography is constructed by the recorded feedback controller output.

Feedback bandwidth

There is always a time delay (τ_0) in feedback control. This time delay and other factors which will be specified later limit the maximum possible imaging rate R_{\max} . A quantitative relationship between R_{\max} and these limiting factors is given below. For simplicity, it is assumed that the sample surface profile in the x-z plane has a sinusoidal shape with a periodicity λ and height h_0 . When the sample-stage scanner is moved in the x-direction at velocity V_s , the sample height h under the cantilever tip changes with time as

$$h(t) = (h_0/2) \times [\sin(2\pi ft) + 1], \quad (1)$$

where $f = V_s/\lambda$. During feedback scanning, the z-scanner moves in the direction opposite to the sample height so that the sample surface looks flat when viewed from the cantilever. However, because of the time delay τ_0 , the z-scanner moves at feedback frequency f as

$$z(t) = -(h_0/2) \times [\sin(2\pi ft - \theta) + 1], \quad (2)$$

where $\theta = 2\pi f\tau_0$. Therefore, the sample surface when viewed from the cantilever does not look perfectly flat but varies with time as

$$S(t) = h(t) + z(t) = h_0 \sin(\theta/2) \cos(2\pi ft - \theta/2). \quad (3)$$

The deviation signal $S(t)$ is feedback error. When the cantilever free oscillation amplitude and the amplitude set point are set at A_0 and $A_s (= rA_0; 0 < r < 1)$, respectively, the cantilever tip in contact with the sample surface is pushed upward by the sample to an extent of $D(t) \equiv S(t) + A_0(1 - r)$ provided that the sample is more rigid than the cantilever.

The feedback bandwidth f_B , which is a value characterizing the speed performance of feedback operation in the AFM system, is usually defined by the feedback frequency at which a 45° phase delay occurs in the feedback scan. Thus, $f_B = 1/(8\tau_0)$. Because the feedback frequency f should not exceed f_B , the condition $f < f_B$ holds, which limits the scan speed V_s as $V_s < \lambda f_B$. By all our efforts to increase the response speed of all devices contained in the feedback loop, particularly of the mechanical devices (i.e., cantilever and scanner), f_B is now enhanced up to ~ 110 KHz. For a scan size in the x-direction W and number of scan lines N , the maximum possible imaging rate R_{\max} is given by $R_{\max} = (\lambda f_B)/(2WN)$ when no sample fragility is considered. For example, for $f_B = 110$ KHz, $W = 200$ nm, $N = 100$, and $\lambda = 10$ nm, we obtain $R_{\max} = 27.5$ frames/s (fps).

Sample fragility as a limiting factor of imaging rate

Because of the feedback error, the cantilever tip taps more strongly as it scans a sample surface that is increasing height (i.e., as the tip is heading “uphill” on the surface), and more weakly as it scan a sample surface that is decreasing in height (i.e., heading “downhill”). The maximum tapping force F_{\max} is approximately expressed as

$$F_{\max} = (k_c/Q_c) \times [A_0(1 - r) + h_0 \sin(\theta/2)], \quad (4)$$

where k_c and Q_c are the spring constant and quality factor in water of the cantilever, respectively. The degree of sample fragility can be expressed in several ways. For example, sample fragility can be expressed as the maximum possible tapping force F_0 under which the sample still retains its full biological function. The condition $F_0 > F_{\max}$ and eq. (4) determine the maximum possible phase delay θ_{\max} for given values of k_c , Q_c , A_0 , h_0 , and r . This θ_{\max} modifies R_{\max} as

$$R_{\max} = (2\lambda f_B \theta_{\max}) / (\pi WN). \quad (5)$$

Another factor that determines θ_{\max} arises from the condition that the cantilever deflection $D(t)$ should always be positive. When $D(t) < 0$, and when no adhesive force is exerted between the tip and sample, the tip loses contact with the sample surface at its bottom swing of oscillation. When the tip completely detaches from the sample surface, the error signal becomes saturated at $A_0(1 - r)$, regardless of the tip’s distance from the sample surface. In

order for the tip to lightly tap the sample surface, the magnitude of $A_0(1-r)$ has to be set at a small value. When the error signal is saturated under this light-tapping condition, it takes time for the tip to land on the surface again, i.e., “parachuting” occurs. During parachuting, no information on sample topography is obtained. The condition that $D(t)$ should always be positive results in

$$A_0(1-r) - h_0 \sin(\theta/2) > 0. \quad (6)$$

For example, for $A_0 = 1$ nm, $h_0 = 5$ nm, and $r = 0.8$, eq. (6) gives $\theta_{\max} < 4.6^\circ$. Therefore, the maximum possible imaging rate is reduced to $\sim 0.1 \times (\lambda f_B)/(2WN)$. Thus, this parachuting problem is the largest obstacle in achieving a high imaging rate under light-tapping conditions. However, this difficult problem has been solved by a new feedback controller (a dynamic proportional-integral-derivative (PID) controller) we developed [25], in which the feedback gain is automatically increased when A exceeds A_s (i.e., when the tip is scanning at a downhill region on the sample).

Effect of tip tapping on sample

HS-AFM was developed with the goal of observing dynamic events of functioning biomolecules. Therefore, we must quantitatively consider any adverse effects of the tip tapping on the sample. Note that the mechanical quantity that affects the sample (i.e., causes a momentum change) is not the force itself but the impulsive force (the product of the force acting on the sample and the time for which the force acts). The small cantilevers, which we have been using routinely, have $k_c = 0.2$ N/m, $f_c = 3.5$ MHz in air and 1.2 MHz in water, and $Q_c = 2$ in water. As described later, non-invasive imaging can be carried out for various proteins under conditions of $A_0 = 1$ nm, $r = 0.8-0.9$, and $\theta = 20^\circ$. Under these conditions, the magnitude of the maximum tapping force estimated using eq. (4) is ~ 100 pN for a typical protein height of $h_0 \sim 5$ nm. However, the force acting time is short (~ 100 ns or less). Thus, the magnitude of the impulsive force is small.

The effect of tip tapping on the sample can also be estimated from the energy loss of an oscillating cantilever. When a cantilever with $k_c = 0.2$ N/m is oscillated at $A_0 = 1$ nm, its mechanical energy is only $\sim 24 k_B T$, where k_B is Boltzmann’s constant and T is 300 K. This value is comparable to the energy of ATP hydrolysis, $\sim 20 k_B T$. Even when this amount of energy is completely lost and used to excite the sample, the energy would be distributed into many degrees of freedom within the tapped portion of the sample and quickly dissipate into more degrees of freedom, including those of surrounding water molecules (as discussed below). In actual imaging experiments, such events of complete energy loss would happen only very rarely, if at all, and overall, the cantilever oscillation amplitude is maintained at $r \times A_0 = 0.8-0.9$ nm. On average, the amount of energy loss after each tap is very small: $\frac{1}{2} k_c A_0^2 (1 - r^2) / Q_c = 2.3-4.4 k_B T$.

The tip oscillating at high f_c in water iteratively taps the sample. When one image is captured for an area of $W_x \times W_y$ nm² at an imaging rate R , a molecule with a top surface area (A_{top} nm²) perpendicular to the tip is tapped $f_c/R \times A_{\text{top}}/(W_x W_y)$ times per frame. For example, under the conditions ($f_c \sim 1$ MHz, $R = 12.5$ fps, and $W_x \times W_y = 45 \times 22$ nm²) used for non-invasive imaging of axle-less F₁-ATPase (i.e., the γ subunit is removed from F₁-ATPase) [28], one molecule of axle-less F₁-ATPase ($A_{\text{top}} \sim 100$ nm²) is tapped $\sim 8,000$ times per frame and ~ 4 million times in total during the successive 40 s imaging. Nevertheless, the axle-less F₁-ATPase is fully functional throughout the imaging, as shown later. This result clearly indicates that the energy transferred from the oscillating tip to the sample never accumulates in the sample but instead dissipates quickly (much faster than the oscillation period of the cantilever, ~ 1 μ s).

Recent progress in bioimaging by HS-AFM

In 2008, HS-AFM was started to be utilized to solve biological issues that had to date been difficult or impossible to address by other methods. Since then, the number of publications on bioimaging by HS-AFM has gradually increased, increasing rapidly in the last three years (see Review [31]). The bioimaging studies conducted thus far have covered a wide range of dynamic molecular processes and structure dynamics, which can be classified into (i) structure dynamics of proteins in action [26-28, 34-37], (ii) selfassembly processes [31, 38, 39], (iii) dynamic protein-protein and protein-DNA interactions [40-44], (iv) diffusion processes [30, 45-47], (v) molecular processes associated with enzymatic reactions [31, 32, 48-50], and (vi) dynamics occurring with DNA origamis [51-55]. Moreover, nonbiological dynamic phenomena, such as the photodegradation of single chains of a chiral helical π -conjugated polymer [56], the phase transition of detergent aggregates [57], and dissolution of photoresists [58] have been captured on video. Below we describe two of our own recently published imaging studies of proteins in action.

Rotary catalysis of axle-less F₁-ATPase

The minimum unit of F₁-ATPase, $\alpha_3\beta_3\gamma$ subcomplex, is a rotary motor that retains full ATPase activity (Fig. 2a) [59-61]. The coiled-coil part of the rotary shaft γ is inserted in the central cavity formed by a stator ring $\alpha_3\beta_3$, where three α and three β subunits are arranged alternately [62]. Three ATP binding sites are located at the α - β interfaces, mainly in the β subunits. The rotation of γ occurs in the counterclockwise direction as viewed from the exposed globular portion of γ (or from the C-terminal side of $\alpha_3\beta_3$). In the ATPase cycle, three β subunits take different chemical states: ATP-bound, ADP-bound, and nucleotide-free (empty) states [59, 62]. Each chemical state cyclically propagates among the three β subunits (i.e., rotary catalysis occurs). Therefore, there is strong cooperativity among the β subunits. How is this cooperativity created? There is no direct contact between any pairs of β subunits

and at any instance the β - γ interaction is always different for the three β subunits because γ has no symmetry. Considering these facts, Wang and Oster proposed that interactions with γ control and determine the conformational and catalytic states of individual β subunits [63]. This idea was reinforced by studies showing that backward mechanical rotation of γ with external force reverses the chemical reaction toward ATP synthesis [64, 65], whereas forced forward rotation accelerates ATP binding [66]. This view was challenged by the finding that even when γ is shortened so that most γ - β interaction sites are eliminated, the short γ still rotates unidirectionally [67]. However, in single-molecule optical microscopy, there is no way to observe the rotary catalysis after the complete removal of γ . Thus, we exploited the power of HS-AFM to solve this issue [28].

$\alpha_3\beta_3$ with Lys₇-tags at the N-termini of its β subunits was covalently immobilized on an amino-reactive mica surface. An image of the C-terminal side of $\alpha_3\beta_3$ without nucleotide shows a pseudo-sixfold symmetric ring (Fig. 2b). Each subunit has an upwardly protruding portion at the inner top side of the ring, but these portions are higher at three alternately arranged subunits than at the other three. Comparison of this image with a simulated AFM image (Fig. 2d) constructed from a crystal structure of nucleotide-free $\alpha_3\beta_3$ (PDB code, 1SKY) (Fig. 2c) [68] revealed that the three subunits showing higher protrusions are the three β subunits. In 1 mM AMP-PNP, the shape of $\alpha_3\beta_3$ became triangular and the central hole became obscure (Fig. 2e). Only one subunit had a higher protrusion together with an outwardly extended distal portion, which was identified to be an empty β subunits by comparison of the experimental AFM image with a simulated one (Fig. 2g) constructed from a crystal structure of nucleotide-bound $\alpha_3\beta_3\gamma$ subcomplex (PDB code: 1BMF) [62] from which γ was removed (Fig. 2f). In addition, the two subunits with retracted distal portions were identified to be nucleotide-bound β 's.

When imaged in 2–4 μ M ATP at 12.5 fps, distinct conformational dynamics appeared at the β subunits (Fig. 3a shows images obtained in 2 μ M ATP; Movie S1 was acquired in 3 μ M ATP). Each β subunits exhibited a conformational transition between the outwardly extended high state (open (O) state) and the retracted low state (closed (C) state). The following prominent features were observed: (i) only one β subunit assumes the O state, and (ii) when the O-to-C transition occurs at one β subunit, the opposite C-to-O transition occurs simultaneously at its counterclockwise neighbour β subunit in most cases. Thus, the O conformation propagates counterclockwise (as noted by the changing locations of the highest pixels, each marked with a red circle, in Fig. 3a). The ATP hydrolysis rates at 2, 3, and 4 μ M ATP were approximately one-third the rates of conformational propagation at 2, 3, and 4 μ M ATP, respectively. Thus, the conformational propagation is tightly coupled with the ATPase reaction. As shown in Fig. 3b, the cumulated angle of the highest pixel with discrete 120° steps revolves linearly with time until the end of imaging (40 s total). Thus, the function of $\alpha_3\beta_3$ is completely retained throughout the imaging. As mentioned above, the $\alpha_3\beta_3$ molecule is tapped with the oscillating tip \sim 4 million times in total during this successive imaging.

These dynamic transitions indicate that the O-to-C transition occurs when ATP is bound to an empty β subunit while the C-to-O transition occurs when an ADP-bound β subunit releases ADP. So, the empty, ADP-bound, and ATP-bound β subunits are arranged counterclockwise in this order, and therefore, the observed conformational propagation demonstrates rotary catalysis by the $\alpha_3\beta_3$ subcomplex. Thus, we reach the important conclusion that the intrinsic cooperativity responsible for torque generation to rotate γ is elicited through β - β interplay alone, and that γ passively undergoes torque to rotate [28].

Bacteriorhodopsin in response to light

Bacteriorhodopsin (bR) is a light-driven proton pump, transferring protons across the membrane from the cytoplasmic side to the extracellular side [69, 70]. bR comprises seven transmembrane α -helices (named A–G) surrounding the retinal chromophore covalently bound to Lys216 via a protonated Schiff base [71, 72]. In the native membrane (referred to as the purple membrane), bR assembles into trimers, which are arranged in a hexagonal lattice. bR has been extensively studied by optical spectroscopy techniques. Upon absorption of light, photoisomerization from the all-*trans* conformation to the 13-*cis* conformation of the retinal takes place. This isomerization induces proton transfer from the Schiff base to Asp85, which triggers a cascade of changes in the bR structure. A series of intermediates designated J–O are defined, among which M (M410) having an absorption peak at 410 nm and the longest lifetime is the only intermediate containing a deprotonated Schiff base [70]. In contrast to this well-defined spectroscopy of bR during its photocycle, the overall dynamic structural change in bR upon photoactivation has long been elusive, despite the establishment of detailed static structure in the unphotolyzed state by X-ray crystallography and electron microscopy [73-75]. Thus, bR is one of the best targets for which the power of HS-AFM may be demonstrated.

The photocycle of wild-type (WT) bR at neutral pH proceeds very quickly (~ 10 ms). To slow down the photocycle, we used the D96N bR mutant which has a longer photocycle (~ 10 s at pH 7) but still acts as a proton pump [76]. Native purple membranes containing D96N bR were directly placed on a bare mica surface. Fig. 4a shows successive images of the D96N mutant at the cytoplasmic surface captured at 1 fps [26]. Upon illumination with green light (532 nm, 0.5 μ W), bR markedly changed its structure (as observed by comparison of images at 1 and 2 s) and returned to the ground state within a few seconds after illumination was discontinued. This structural change was specifically induced by green light, not by blue or red light, which is consistent with the fact that bR in the ground state effectively absorbs green light. The centers of mass of all activated bR monomers moved outward by 0.7–0.8 nm from the center of the respective trimers and rotated counterclockwise by 7–8° around the center of the respective trimers. The images shown in Fig. 4b and 4c are averaged images under dark and illumination conditions, respectively (also see Movie S2); the averaging was performed using several trimers appearing in each frame, considering the hexagonal lattice arrangement of the trimers. From these images, it is evident that each protrusion is split into

larger and smaller sections (arrows 1 and 2) upon light illumination. Compared with the atomic model of the α -helical cytoplasmic ends in the unphotolyzed state [72], the protruding areas around helices E and F shift outward from the trimer centre under illumination. Therefore, the protrusion movement visualized here is ascribed to the displacement of the E–F loop. The minor protrusion (arrow 2) likely corresponds to the position around helices A and B. Note that owing to indiscernible alterations at the extracellular surface, the overall position of each bR molecule does not change. The photoactivated state observed by HS-AFM was attributed to the spectroscopically identified M_N intermediate [35] (it exhibits outward tilt of helix F similar to that of N state of WT while the Schiff-base is still deprotonated like the precedent M state because of the absence of the proton donor residue (Asp96) for the Schiff base). Thus, the photo-induced structural change in bR, which has long been studied but elusive, is now clearly revealed by direct visualization with HS-AFM.

As a result of the outward displacement, nearest-neighbor bR monomers (one set is circled in light-blue circle in the image at 1 s in Fig.4a), each belonging to a different adjacent trimer (shown by the three white circles), appear to transiently assemble (as indicated by the light-blue circle in the image at 2 s). We define the triad of nearest-neighbor monomers belonging to different trimers as a “trefoil”, to distinguish such a structure from the original trimers. To investigate the possible effect of bR-bR interaction within a trefoil on the photocycle, bR was illuminated with green light of varying intensity (0.007–0.5 μ W). Under weak illumination, only one monomer in each trefoil was activated in most cases. When only one monomer was activated in a trefoil, it decayed with a time constant of 7.3 ± 0.58 s. In contrast, under stronger illumination, two or three monomers within a trefoil tended to be activated together. Interestingly, the decay of each monomer markedly depended on the order of its activation: the monomer that was activated last among the activated monomers in a trefoil decayed with a shorter time constant of 2.0 ± 0.16 s, whereas the decay kinetics of the monomers activated earlier did not follow a single exponential, and the average decay time lengthened to ~ 13 s. Thus, bR-bR interaction within an illuminated trefoil creates both positive and negative cooperative effects in the decay kinetics as the initial bR recovers.

In contrast to previous expectations [77, 78], these cooperativities do not occur within a trimer, but within a trefoil. This finding was made possible by closely looking at individual bR molecules at high spatial resolution, in real space and real time. It is difficult to imagine how such cooperativity could be observed using techniques other than HS-AFM.

Unique features of HS-AFM imaging

As demonstrated above, the entire structure of a protein molecule and its minute changes with time can be captured in an AFM movie. Unlike fluorescence microscopy, wherein the subset of molecular events observed is dependent on the selected site where the probe is placed (and hence, dynamic events to be observed are preselected), various dynamic events of a molecule appear in a molecular movie without preselection. Therefore, we can have a great chance of

learning multiple molecular actions in one imaging experiment. Moreover, molecular actions that appear in a video can often be interpreted in a straightforward manner, without intricate analyses and interpretations, leading to convincing, if not irrefutable, conclusions. These excellent features of HS-AFM imaging significantly facilitate and accelerate our understanding of the functional mechanisms of proteins.

However, HS-AFM often achieves this superiority at the cost of intensive sample preparation. For successful visualization of dynamic events in biomolecular systems, certain conditions are often required of the sample preparation, particularly for the substrate surface on which sample molecules are placed. The substrate surface must have an appropriate affinity for the molecules. To observe dynamic interactions between different species of molecules, selective attachment of one of the species of molecules to a surface is required. Otherwise, there is no chance to observe their interaction. The surface must be flat in HS-AFM, unlike fluorescence microscopy. Moreover, in AFM (and HS-AFM), the sample can be viewed from only one direction, that is, perpendicular to the surface. Therefore, to observe specific molecular features, molecules sometimes have to be oriented selectively on the surface, as in the case of the observation of myosin V molecules walking on an actin filament [27]. Methods that are used to fulfill these conditions are described in articles [32, 79, 80].

Future prospects of HS-AFM studies

Dynamic imaging of isolated biomolecular systems

Various bioimaging studies using HS-AFM have been undertaken in the recent years. Nonetheless, there are countless biomolecular systems remaining to be imaged. Even for biomolecular systems that have already been studied in detail by other approaches, HS-AFM allows us to inquire into more details or questions that have been difficult or impossible to address by other methods, giving us a great chance of making unexpected new findings. This is indeed exemplified in our studies on F_1 -ATPase and bR, as described above, as well as myosin V [27] and cellulase [29]. Importantly, the HS-AFM instrument we have developed is now commercially available from the Research Institute of Biomolecule Metrology, Inc. (Tsukuba, Japan). Small cantilevers made of silicon nitride (9–10 μm long, 2 μm wide and 130 nm thick; BL-AC10DS, Olympus, Tokyo) with $f_c = 1.5$ MHz in air and 0.6 MHz in water, $k_c = 0.1$ N/m, and a quality factor $Q_c \sim 2$ in water are already commercially available. Smaller cantilevers are also being commercialized by NanoWorld (Neuchâtel, Switzerland). Thus, there is no doubt that continued and expanded exploration of dynamic HS-AFM imaging will be carried out for a wide range of biomolecular systems in the near future, which will accelerate and cultivate a better understanding of how biomolecules function. Thereby, HS-AFM will transform traditional structural biology and single-molecule biophysics.

Dynamic imaging of molecules on higher order structures

The fast scanners that we have developed are optimized for high-speed imaging of isolated biomolecules; their resonant frequencies are very high, but the scan range is limited to 1 μm , 4 μm , and 0.8–1 μm in the x-, y-, and z-directions, respectively (when 100 V is applied at maximum). Therefore, large samples such as live bacterial and mammalian cells have not been able to be imaged by HS-AFM until recently. To overcome the scan range limitation, we have recently developed a wide-area scanner that can be displaced up to 43 μm in the x- and y-directions and 2.5–4 μm in the z-direction (when 100 V is applied at maximum). The resonant frequency of these x- and y-scanners is low (~ 1.6 KHz), but can be extended to ~ 10 kHz by an inverse compensation-based active damping technique. The resonant frequency of the z-scanner (50–100 kHz) is determined by the piezoactuator used (and hence approximately by the maximum possible displacement). This resonance is removed by the previously developed Q-control technique [24], but there is no way to extend the bandwidth at present. Using this scanner and another medium-range scanner, images of whole live bacterial cells were recently acquired. After taking an image of an entire magnetic bacterial cell, a localized portion of its outer surface was imaged fast, visualizing porin molecules that were densely packed but rapidly diffusing [45]. This ability to acquire wide-range images will create a new opportunity to observe the dynamics of molecules on higher order structures such as live mitochondria, nuclei, and neuronal spines. Given that the functional dynamic processes of molecules and molecular assemblies occurring on these surfaces are largely unknown, HS-AFM will open new avenues for cell biology as well.

Imaging of dynamics of mammalian cells

In our currently developed HS-AFM method, the feedback operation is continuously performed at every point on the sample surface. Therefore, it takes a longer time to acquire an image of a larger object. However, single-nanometer resolution often is not needed in the imaging of cell morphology. If the feedback operation is performed only at surface points corresponding to pixels of an image to acquire, the imaging time can be significantly reduced. This type of feedback operation is already employed in peak-force mode AFM [81] and in hopping mode [82] (also called AC-mode [83] or pulse mode [84, 85]) scanning ion conductance microscopy. The cantilever base or the sample stage is moved up and down at a hopping frequency f_H in a relatively large hopping amplitude A_H so that the probe is intermittently brought into contact with, or close to, the sample surface. The feedback scan is performed only when the probe tip is retracted from the sample surface. This technique can be implemented in HS-AFM, allowing much faster acquisition of the entire image of a mammalian cell with spatial resolution much higher than that of optical microscopy.

The imaging rate R for this type of HS-AFM is determined by $R = f_H / (N_x \times N_y)$, where N_x and N_y are the number of pixels in the x- and y-directions, respectively. For example, in the case of a typical z-scanner having a resonant frequency $f_z = 50$ kHz and a maximum

displacement $4.3 \mu\text{m}$ at 100 V , we can use $f_H \sim 30 \text{ kHz}$. Therefore, a $10 \times 10 \mu\text{m}^2$ area can be imaged at 0.75 fps with $N_x \times N_y = 200 \times 200$ (pixel size, 50 nm), provided that the z-scanner retraction can be performed quickly after detection of tip-sample contact. However, the z-scanner cannot respond quickly even when its quality factor Q_z is reduced to ~ 1 (the response time $Q_z/(\pi f_z) \sim 6.4 \mu\text{s}$). When $A_H = 100 \text{ nm}$ is used, the z-scanner moves down further during this time delay, and therefore, the sample is indented $\sim 10 \text{ nm}$ or more by the tip. This problem can be solved by the use of a z-scanner to which an additional piezoactuator with a high resonant frequency ($\sim 1 \text{ MHz}$) is attached; with this additional piezoactuator, the z-scanner can be retracted immediately after detection of tip-sample contact.

Funding

This work was supported by a grant-in-aid for Basic Research S (20221006 and 24227005) from the MEXT, Japan, by a Knowledge Cluster Initiative Project, and by a CREST project of the Japanese Science and Technology Agency.

Acknowledgments

I would like to thank Takayuki Uchihashi, Noriyuki Kodera, Daisuke Yamamoto, Hayato Yamashita, Mikihiro Shibata, Ryota Iino, Hiroyuki Noji, Hideki Kandori, and many present and past students in my lab for collaborations or discussions on topics described in this review. I also thank Simon Scheuring for averaging AFM images of bR.

Legends for Figures

Fig.1. Schematic of tapping-mode AFM setup. The cantilever is vertically oscillated at its first resonant frequency. The cantilever deflection is detected by the optical beam deflection (OBD) detector comprised of the laser diode and the split photodetector. The differential signal from the split photodetector is converted to an amplitude signal by the amplitude detector. The detected amplitude signal is compared with the predetermined set point, and their difference (error signal) is processed (mainly integrated) by the PID feedback controller to produce a driving signal for displacing the z-scanner so that the error signal approaches zero. By this control, the oscillation amplitude of the cantilever (and hence, the vertical tip-sample interaction force) is mostly maintained constant during the lateral scanning of the sample stage. The D/A converters implemented in the PC output drive signals to laterally move the sample stage, while the A/D converter records the feedback controller output representing the sample height.

Fig. 2. AFM images of $\alpha_3\beta_3$ subcomplex at C-terminal surface. (a) Schematic for F_1 -ATPase. (b) Averaged AFM image obtained in nucleotide-free condition. (c) C-terminal surface of crystal structure of nucleotide-free $\alpha_3\beta_3$ subcomplex. (d) Simulated AFM image of (c). (e)

Averaged AFM image obtained in 1 mM AMP-PNP. (f) C-terminal surface of crystal structure of $\alpha_3\beta_3$ subcomplex obtained in ATP. (g) Simulated AFM image of (f).

Fig. 3. Rotary propagation of conformational change of $\alpha_3\beta_3$ subcomplex at C-terminal surface. (a) Successive images of C-terminal surface of $\alpha_3\beta_3$ subcomplex in 2 μ M ATP, captured by HS-AFM at 12.5 fps. The highest pixel position in each image is marked with the red circle. (b) Time evolution of the cumulated angle of the highest pixel. The inset shows a trajectory, superimposed on an AFM image, of the highest pixels corresponding to the high protrusions of β subunits in the open state.

Fig. 4. Structural change in bR induced by light absorption. (a) Successive high-speed AFM images of the cytoplasmic surface of D96N bR in dark and illuminated conditions, captured at 1 fps. The green bars at 2 and 3 s indicate illumination of 532nm green light with an intensity of 0.5 μ W. A bR trimer is highlighted by the white triangle in the image at 0 s. In the image at 1 s, three adjacent trimers are encircled with white circles, while a trefoil comprised of three nearest-neighbor monomers, each belonging to one of the encircled trimers, is indicated with the light-blue circle. The same trefoil is encircled in light blue in the images at 2 s and 3 s. (b) Averaged AFM image of trimer in dark conditions. (c) Averaged AFM image of trimer under illumination. Under illumination, the protrusion is split into larger (arrow 1) and smaller (arrow 2) sections.

References

- 1 Huang B, Bates M, and Zhuang X (2009) Super-resolution fluorescence microscopy. *Annu. Rev. Biochem.* **78**, 993–1016.
- 2 De Jonge N, and Ross F M (2011) Electron microscopy of specimens in liquid. *Nat. Nanotechnol.* **6**, 695–704.
- 3 Binnig G, Quate C F, and Gerber Ch (1986) Atomic force microscope. *Phys. Rev. Lett.* **56**, 930–933.
- 4 Müller D J, and Dufrêne Y F (2008) Atomic force microscopy as a multifunctional molecular toolbox in nanobiotechnology. *Nat. Nanotechnol.* **3**, 261–269.
- 5 Müller D J, Helenius J, Alsteens D, and Dufrêne Y F (2009) Force probing surfaces of living cells to molecular resolution. *Nat. Chem. Biol.* **5**, 383–390.
- 6 Müller D J, Janovjak H, Lehto T, Kuerschner L, and Anderson K (2002) Observing structure, function and assembly of single proteins by AFM. *Prog. Biophys. Mol. Biol.* **79**, 1–43.
- 7 Scheuring S and Sturgis J N (2005) Chromatic adaptation of photosynthetic membranes. *Science* **309**, 484–487.

- 8 Nakajima H, Kunioka Y, Nakano K, Shimizu K, Seto M, and Ando, T (1997) Scanning force microscopy of the interaction events between a single molecule of heavy meromyosin and actin. *Biochem. Biophys. Res. Commun.* **234**, 178–182.
- 9 Williams M, Fowler S B, Robert B, Best R B, Toca-Herrera J L, Scott K A, Steward A, and Clarke J (2003) Hidden complexity in the mechanical properties of titin. *Nature* **422**, 446–449.
- 10 Dague E, Alsteens D, Latgé J-P, Verbelen C, Raze D, Baulard A R, and Dufrêne Y F (2007) Chemical force microscopy of single live cells. *Nano Lett.* **7**, 3026–3030.
- 11 Touhami A, Nysten B, Dufrêne Y F (2003) Nanoscale mapping of the elasticity of microbial cells by atomic force microscopy. *Langmuir* **19**, 4539–4543.
- 12 Stewart M P, Helenius J, Toyoda Y, Ramanathan S P, Müller D J, and Hyman A A (2011) Hydrostatic pressure and the actomyosin cortex drive mitotic cell rounding. *Nature* **469**, 226–230.
- 13 Drake B, Prater C B, Weisenhorn A L, Gould S A C, Albrecht T R, Quate C F, Cannell D S, Hansma H G, and Hansma P K (1989) Imaging crystals, polymers, and processes in water with the atomic force microscope. *Science* **243**, 1586–1589.
- 14 Häberle W, Höber J K H, Ohnesorge F, Smith D P E, and Binnig G (1992) In situ investigations of single living cells infected by viruses. *Ultramicroscopy* **42–44**, 1161–1167.
- 15 Ohnesorge F, Heckl W M, Häberle W, Pum D, Sara M, Schindler H, Schilcher K, Kiener A, Smith D P E, Sleytr U B, and Binnig G (1992) Scanning force microscopy studies of the S-layers from *Bacillus coagulans* E38-66, *Bacillus sphaericus* CCM2177 and of an antibody binding process. *Ultramicroscopy* **42–44**, 1236–1242.
- 16 Binnig G (1992) Force microscopy. *Ultramicroscopy* **42–44**, 7–15.
- 17 Ando T, Uchihashi T, and Fukuma T (2008) High-speed atomic force microscopy for nano-visualization of dynamic biomolecular processes. *Prog. Surf. Sci.* **83**, 337–437.
- 18 Walters D A, Cleveland J P, Thomson N H, Hansma P K, Wendman M A, Gurley G, and Elings V (1996) Short cantilevers for atomic force microscopy. *Rev. Sci. Instrum.* **67**, 3583–3590.
- 19 Kitazawa M, Shiotani K, and Toda A (2003) Batch fabrication of sharpened silicon nitride tips. *Jpn. J. Appl. Phys.* **42**, 4844–4847.
- 20 Ando T, Kodera N, Takai E, Maruyama D, Saito K, and Toda A (2001) A high-speed atomic force microscope for studying biological macromolecules. *Proc. Natl. Acad. Sci. USA* **98**, 12468–12472.
- 21 Viani M B, Schäffer T E, Palocz G T, Pietrasanta L I, Smith B L, Thompson J B, Richter M, Rief M, Gaub H E, Plaxco K W, Cleland N, Hansma, H G, and Hansma P K (1999) Fast imaging and fast force spectroscopy of single biopolymers with a new atomic force microscope designed for small cantilevers. *Rev. Sci. Instrum.* **70**, 4300–4303.

- 22 Ando T, Uchihashi T, Kodera N, Miyagi A, Nakakita R, Yamashita H, and Matada K (2005) High-speed AFM for studying the dynamic behavior of protein molecules at work. *e-J. Surf. Sci. Nanotechnol.* **3**, 384–392.
- 23 Fukuma T, Okazaki Y, Kodera N, Uchihashi T, and Ando T (2008) High resonance frequency force microscope scanner using inertia balance support. *Appl. Phys. Lett.* **92**, 243119 (3 pp).
- 24 Kodera N, Yamashita H, and Ando T (2005) Active damping of the scanner for high-speed atomic force microscopy. *Rev. Sci. Instrum.* **76**, 053708 (5 pp).
- 25 Kodera N, Sakashita M, and Ando T (2006) Dynamic proportional-integral-differential controller for high-speed atomic force microscopy. *Rev. Sci. Instrum.* **77**, 083704 (7 pp).
- 26 Shibata M, Yamashita H, Uchihashi T, Kandori H, and Ando T (2010) High-speed atomic force microscopy shows dynamic molecular processes in photo-activated bacteriorhodopsin. *Nat. Nanotechnol.* **5**, 208–212 (2010).
- 27 Kodera N, Yamamoto D, Ishikawa R, and Ando T (2010) Video imaging of walking myosin V by high-speed atomic force microscopy. *Nature* **468**, 72–76.
- 28 Uchihashi T, Iino R, Ando T, and Noji H (2011) High-speed atomic force microscopy reveals rotary catalysis of rotorless F1-ATPase. *Science* **333**, 755–758.
- 29 Igarashi K, Uchihashi T, Koivula K, Wada M, Kimura S, Okamoto T, Penttilä M, Ando T, and Samejima M (2011) Traffic jams reduce hydrolytic efficiency of cellulase on cellulose surface. *Science* **333**, 1279–1282.
- 30 Casuso I, Khao J, Paul-Gilloteaux P, Husain M, Duneau J-P, Stahlberg H, Sturgis J N, and Scheuring S (2012) Characterization of the motion of membrane proteins using high-speed atomic force microscopy. *Nat. Nanotechnol.* **7**, 525–529.
- 31 Ando T (2012) High-speed atomic force microscopy coming of age. *Nanotechnology* **23**, 062001 (27 pp).
- 32 Uchihashi T, Kodera N, and Ando T (2012) Guide to video recording of structure dynamics and dynamic processes of proteins by high-speed atomic force microscopy. *Nat. Protocols* **7**, 1193–1206.
- 33 Zhong Q, Inniss D, Kjoller K, and Elings V B (1993) Fractured polymer/silica fiber surface studied by tapping mode atomic force microscopy. *Surf. Sci.* **290**, L688–L692.
- 34 Shinozaki Y, Sumitomo K, Tsuda M, Koizumu S, Inoue K, and Torimitsu K (2009) Direct observation of ATP-induced conformational changes in single P2X₄ receptors. *PLoS Biol.* **7**, e1000103 (12 pp).
- 35 Shibata M, Uchihashi T, Yamashita H, Kandori, and Ando T (2011) Structural changes in bacteriorhodopsin in response to alternate illumination observed by high-speed atomic force microscopy. *Angew. Chem. Int. Ed.* **50**, 4410–4413.
- 36 Yokokawa M, and Takeyasu K (2011) Motion of the Ca²⁺-pump captured. *FEBS J.* **278**, 3025–3031.

- 37 Miyagi A, Tsunaka Y, Uchihashi T, Mayanagi K, Hirose S, Morikawa K, and Ando T (2008) Visualization of intrinsically disordered regions of proteins by high-speed atomic force microscopy. *Chem. Phys. Chem.* **9**, 1859–1866.
- 38 Milhiet P-E, Yamamoto D, Berthoumieu O, Dosset P, Le Grimellec Ch, Verdier J-M, SMarchal S, and Ando T (2010) Deciphering the structure, growth and assembly of amyloid-like fibrils using high-speed atomic force microscopy. *PLoS ONE* **5**, e13240 (8 pp).
- 39 Giocondi M-C, Yamamoto D, Lesniewska E, Milhiet P-E, Ando T, and Le Grimellec Ch (2010) Surface topography of membrane domains. *Biochim. Biophys. Acta. Biomembranes* **1798**, 703–718.
- 40 Casuso I, Sens P, Rico F, and Scheuring S (2010) Experimental evidence for membrane-mediated protein-protein interaction. *Biophys. J.* **99**, L47–L49.
- 41 Casuso I, Kodera N, Le Grimellec Ch, Ando T, and Scheuring S (2009) High-resolution high-speed contact mode atomic force microscopy movies of purple membrane. *Biophys. J.* **97**, 1354–1361.
- 42 Yamashita H, Voitchovsky K, Uchihashi T, Antoranz Contera S, Ryan J F, and T Ando (2009) Dynamics of bacteriorhodopsin 2D crystal observed by high-speed atomic force microscopy. *J. Struct. Biol.* **167**, 153–158.
- 43 Miyagi A, Ando T, and Lyubchenko Y L (2011) Dynamics of nucleosomes assessed with time-lapse high speed atomic force microscopy. *Biochemistry* **50**, 7901–7908.
- 44 Suzuki Y, Higuchi Y, Hizume K, Yokokawa M, Yoshimura S H, Yoshikawa K, and Takeyasu K (2010) Molecular dynamics of DNA and nucleosomes in solution studied by fast-scanning atomic force microscopy. *Ultramicroscopy* **110**, 682–688.
- 45 Yamashita H, Taoka A, Uchihashi T, Asano T, Ando T, and Fukumori Y (2012) Single molecule imaging on living bacterial cell surface by high-speed AFM. *J. Mol. Biol.* **422**, 300–309.
- 46 Yamamoto D, Uchihashi T, Kodera N, and Ando T (2008) Anisotropic diffusion of point defects in two-dimensional crystal of streptavidin observed by high-speed atomic force microscopy. *Nanotechnol.* **19**, 384009 (9 pp).
- 47 Sanchez H, Suzuki Y, Yokokawa M, Takeyasu K, and Wyman C (2011) Protein-DNA interactions in high speed AFM: single molecule diffusion analysis of human RAD54. *Integr. Biol.* **3**, 1127–1134.
- 48 Igarashi K, Koivula A, Wada M, Kimura S, Penttilä M, and Samejima M (2009) High speed atomic force microscopy visualizes processive movement of *Trichoderma reesei* cellobiohydrolase I on crystalline cellulose. *J. Biol. Chem.* **284**, 36186–36190.
- 49 Gilmore J L, Suzuki Y, Tamulaitis G, Siksnys V, Takeyasu K, and Lyubchenko Y L (2009) Single-molecule dynamics of the DNA–*EcoRII* protein complexes revealed with high-speed atomic force microscopy. *Biochemistry* **48**, 10492–10498.

- 50 Suzuki Y, Gilmore J L, Yoshimura S H, Henderson R M, Lyubchenko Y L, and Takeyasu K (2011) Visual analysis of concerted cleavage by type IIF restriction enzyme SfiI in subsecond time region. *Biophys. J.* **101**, 2992–2998.
- 51 Endo M, Hidaka K, and Sugiyama H (2011) Direct AFM observation of an opening event of a DNA cuboid constructed via a prism structure. *Org. Biomol. Chem.* **9**, 2075–2077.
- 52 Endo M, Katsuda Y, Hidaka K, and Sugiyama H (2010) Regulation of DNA methylation using different tensions of double strands constructed in a defined DNA nanostructure. *J. Am. Chem. Soc.* **132**, 1592–1597.
- 53 Sannohe Y, Endo M, Katsuda Y, Hidaka K, and Sugiyama H (2010) Visualization of dynamic conformational switching of the G-quadruplex in a DNA nanostructure. *J. Am. Chem. Soc.* **132**, 16311–16313.
- 54 Tanaka F, Mochizuki T, Liang X, Asanuma H, Tanaka S, Suzuki K, Kitamura S, Nishikawa A, Ui-Tei K, and Hagiya M (2010) Robust and photocontrollable DNA capsules using azobenzenes. *Nano Lett.* **10**, 3560–3565.
- 55 Wickham F J S, Endo M, Katsuda Y, Hidaka K, Bath J, Sugiyama H, and Turberfield A J (2011) Direct observation of stepwise movement of a synthetic molecular transporter. *Nat. Nanotechnol.* **6**, 166–169.
- 56 Shinohara K, Kodera N, and Oohashi T (2010) Single-molecule imaging of photodegradation reaction in a chiral helical π -conjugated polymer chain. *J. Polym. Sci. A* **48**, 4103–4107.
- 57 Inoue S, Uchihashi T, Yamamoto D, and Ando T (2011) Direct observation of surfactant aggregate behavior on a mica surface using high-speed atomic force microscopy. *Chem. Commun.* **47**, 4974–4976.
- 58 Itani T, and Santillan J J (2010) *In situ* characterization of photoresist dissolution. *Appl. Phys. Express* **3**, 061601 (3 pp).
- 59 Gresser M J, Myers J A, and Boyer P D (1982) Catalytic site cooperativity of beef heart mitochondrial F₁ adenosine triphosphatase. Correlations of initial velocity, bound intermediate, and oxygen exchange measurements with an alternating three-site model. *J. Biol. Chem.* **257**, 12030–12038.
- 60 Noji H, Yasuda R, Yoshida M, and Kinosita K Jr (1997) Direct observation of the rotation of F₁-ATPase. *Nature* **386**, 299–302.
- 61 Yasuda R, Noji H, Kinosita K Jr, and Yoshida M (1998) F₁-ATPase is a highly efficient molecular motor that rotates with discrete 120° steps. *Cell* **93**, 1117–1124.
- 62 Abrahams J P, Leslie A G, Lutter R, and Walker J E (1994) Structure at 2.8 Å resolution of F₁-ATPase from bovine heart mitochondria. *Nature* **370**, 621–628.
- 63 Wang H, and Oster G (1998) Energy transduction in the F₁ motor of ATP synthase. *Nature* **396**, 279–282.
- 64 Itoh H, Takahashi A, Adachi K, Noji H, Yasuda R, Yoshida K, and Kinosita K Jr (2004) Mechanically driven ATP synthesis by F₁-ATPase. *Nature* **427**, 465–458.

- 65 Rondelez Y, Tresset G, Nakashima T, Kato-Yamada Y, Fujita H, Takeuchi S, and Noji H (2005) Highly coupled ATP synthesis by F₁-ATPase single molecules. *Nature* **433**, 773–777.
- 66 Iko Y, Tabata K V, Sakakihara S, Nakashima T, Noji H (2009) Acceleration of the ATP-binding rate of F₁-ATPase by forcible forward rotation. *FEBS Lett.* **583**, 3187–3191.
- 67 Furuike S, Hossain M D, Maki Y, Adachi K, Suzuki T, Kohori A, Itoh H, Yoshida M, and Kinoshita K Jr (2008) Axle-less F₁-ATPase rotates in the correct direction. *Science* **319**, 955–958.
- 68 Shirakihara Y, Leslie A G, Abrahams J P, Walker J E, Ueda T, Sekimoto Y, Kambara M, Kagawa Y, and Yoshida M (1997) The crystal structure of the nucleotide-free alpha 3 beta 3 subcomplex of F₁-ATPase from the thermophilic *Bacillus* PS3 is a symmetric trimer. *Structure* **5**, 825–836.
- 69 Haupts U, Tittor J, and Oesterhelt D (1999) Closing in on bacteriorhodopsin: Progress in understanding the molecule. *Annu. Rev. Biophys. Biomol. Struct.* **28**, 367–399.
- 70 Lanyi J K (2004) Bacteriorhodopsin. *Annu. Rev. Physiol.* **66**, 665–688.
- 71 Kimura Y, Vassilyev D G, Miyazawa A, Kidera A, Matsushima M, Mitsuoka K, Murata K, Hirai T, and Fujiyoshi Y (1997) Surface of bacteriorhodopsin revealed by high-resolution electron crystallography. *Nature* **389**, 206–211.
- 72 Luecke H, Schobert B, Richter H T, Cartailler J P, and Lanyi J K (1999) Structure of bacteriorhodopsin at 1.55 Å resolution. *J. Mol. Biol.* **291**, 899–911.
- 73 Luecke H, Schobert B, Lanyi J K, Spudich E N, and Spudich J L (2001) Crystal structure of sensory rhodopsin II at 2.4 Angstroms: Insights into color tuning and transducer interaction. *Science* **293**, 1499–1503.
- 74 Sass H J, Büldt G, Gessenich R, Hehn D, Neff D, Schlesinger R, Berendzen J, and Ormos P (2000) Structural alterations for proton translocation in the M state of wild-type bacteriorhodopsin. *Nature* **406**, 649–653.
- 75 Subramaniam S, and Henderson R (2000) Molecular mechanism of vectorial proton translocation by bacteriorhodopsin. *Nature* **406**, 653–657.
- 76 Otto H, Marti T, Holz M, Mogi T, Lindau M, Khorana H G, and Heyn M P (1989) Aspartic acid-96 is the internal proton donor in the reprotonation of the Schiff base of bacteriorhodopsin. *Proc. Natl. Acad. Sci. USA.* **86**, 9228–9232.
- 77 Komrakov A Y, and Kaulen A D (1995) M-decay in the bacteriorhodopsin photocycle: effect of cooperativity and pH. *Biophys. Chem.* **56**, 113–119.
- 78 Tokaji Z (1997) Dimeric-like kinetic cooperativity of the bacteriorhodopsin molecules in purple membranes. *Biophys. J.* **65**, 1130–1134.
- 79 Yamamoto D, Nagura N, Omote S, Taniguchi M, and Ando, T (2009) Streptavidin 2D crystal substrates for visualizing biomolecular processes by atomic force microscopy. *Biophys. J.* **97**, 2358–2367.

- 80 Yamamoto D, Uchihashi T, Kodera N, Yamashita H, Nishikori S, Ogura T, Shibata M, and Ando T (2010) High-speed atomic force microscopy techniques for observing dynamic biomolecular processes. *Methods Enzymol.* **475**, 541–564.
- 81 Pittenger B, Erina N, and Su C (2010) Quantitative mechanical property mapping at the nanoscale with Peak Force QNM. *Veeco Application Note* **128**, 1–12.
- 82 Novak P, Li C, Shevchuk A I, Stepanyan R, Caldwell M, Hughes S, Smart T G, Gorelik J, Ostanin V P, Lab M J, Moss G W J, Frolenkov G I, Klenerman D, and Korchev Y E (2009) Nanoscale live-cell imaging using hopping probe ion conductance microscopy. *Nat. Methods* **6**, 279–281.
- 83 Pastré D, Iwamoto H, Liu J, Szabo G, and Shao Z (2001) Characterization of AC mode scanning ion-conductance microscopy. *Ultramicroscopy* **90**, 13–19.
- 84 Happel P, Hoffmann G, Mann S A, Dietzel I D (2003) Monitoring cell movements and volume changes with pulse-mode scanning ion conductance microscopy. *J. Microsc.* **212**, 144–151.
- 85 Mann S A, Hoffmann G, Hengstenberg A, Schuhmann W, and Dietzel I D (2002) Pulse-mode scanning ion conductance microscopy – a method to investigate cultured hippocampal cells. *J. Neurosci. Methods* **116**, 113–117.

Table 1. Feasibility comparison of three types of microscopy

Conditions Microscopy	In-liquid specimen	High spatial resolution	High temporal resolution	Low invasiveness	Direct imaging
Fluorescence Microscopy	○	○	○	○	×
Electron Microscopy	∅	○	∅	×	○
Atomic force Microscopy	○	○	×	∅	○

○, Fully met; ∅, Partially met or conditional; ×, impossible or extensive efforts required to meet

“Direct imaging” means that the morphology of an object itself is resolved.

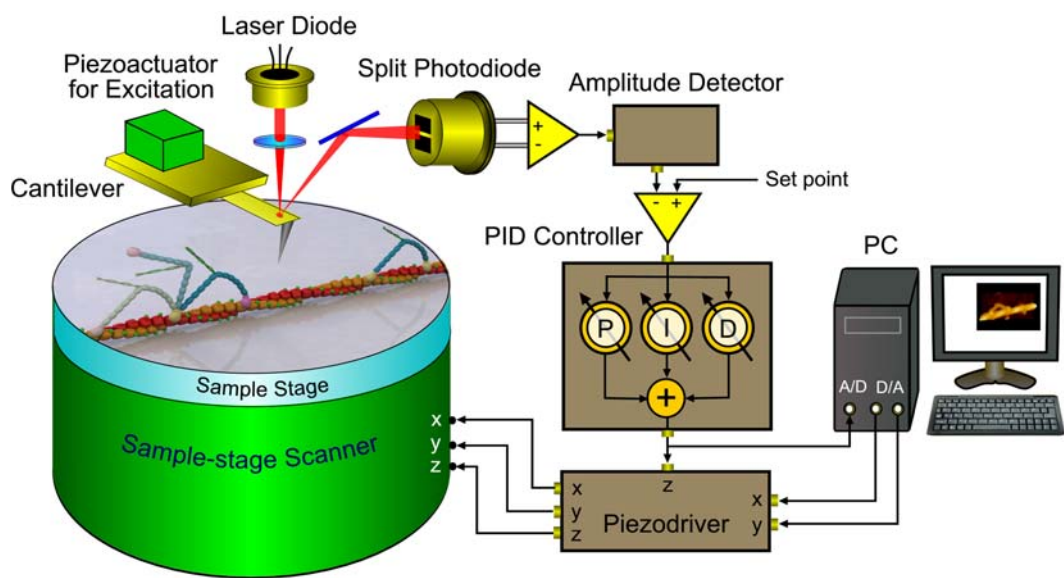


Figure 1

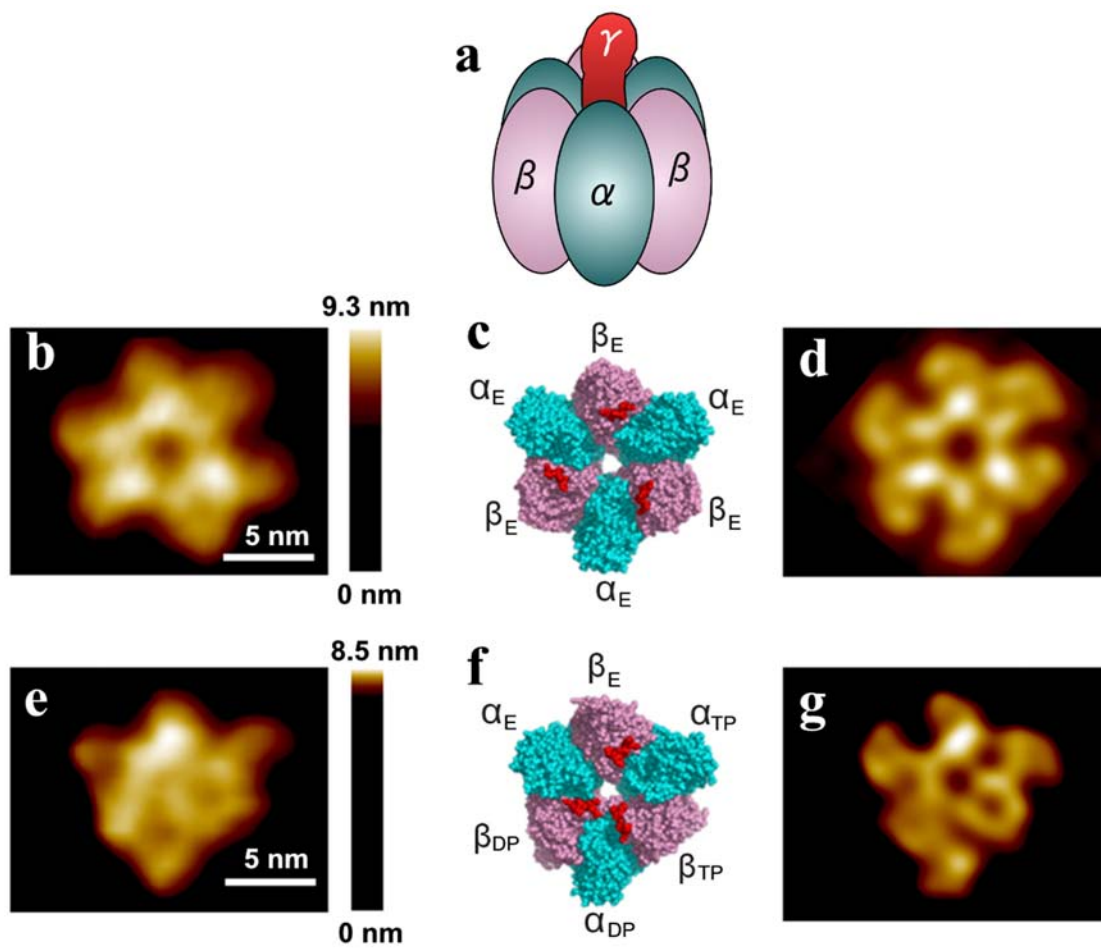


Figure 2

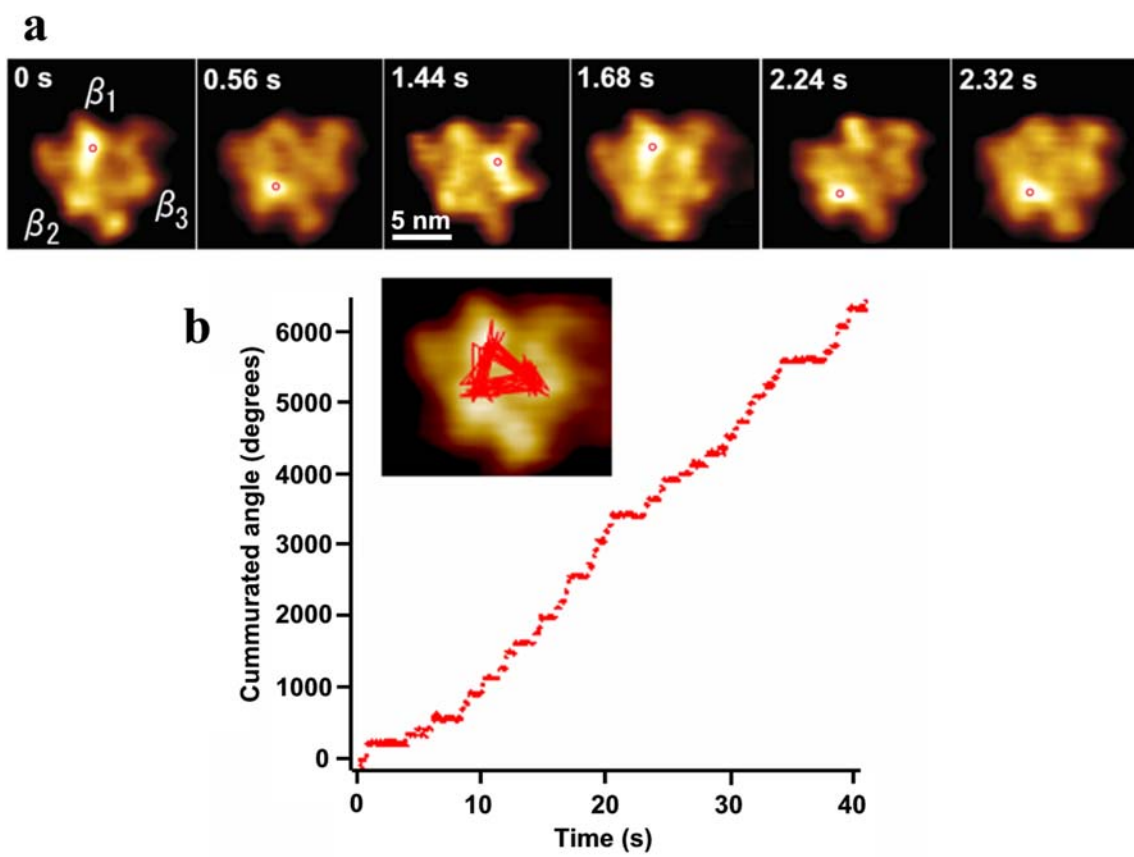


Figure 3

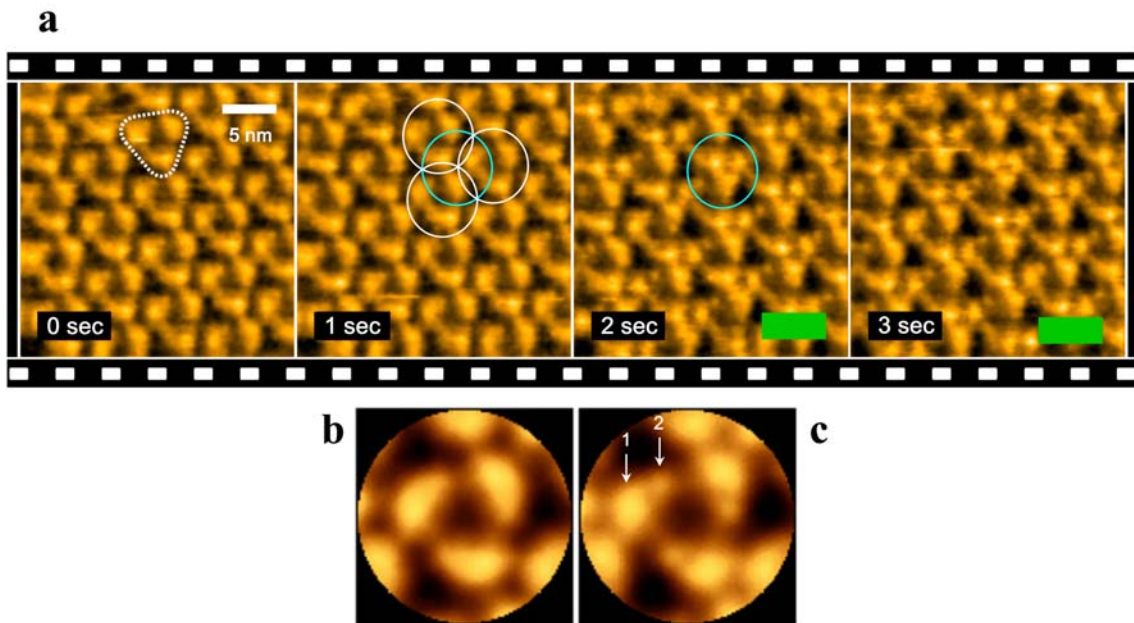


Figure 4